LANGMUIR

pubs.acs.org/Langmuir Article

Role of Water in the Lyotropic Liquid Crystalline Mesophase of Lithium Salts and Non-ionic Surfactants

Ezgi Yılmaz Topuzlu, Halil I. Okur, Burak Ulgut, and Ömer Dag*

Cite This: *Langmuir* 2021, 37, 14443−14453 Read Online

ACCESS | Metrics & More | Article Recommendations | Supporting Information

ABSTRACT: The lyotropic liquid crystalline (LLC) mesophase forms upon evaporation of water from aqueous solutions of LiX salts (X is Cl^-, Br^-, NO_3^-, or SCN^-) and a surfactant [$C_{12}H_{25}(OCH_2CH_2)_{10}OH$, abbreviated as $C_{12}E_{10}$]. The LiX/$C_{12}E_{10}$/H_2O aqueous solutions have been monitored (during evaporation of their excess water to obtain stable LLC mesophases) by gravimetric, spectroscopic, and conductivity measurements to elucidate the role of water in these mesophases. The water/salt molar ratio in stable mesophases changes from 1.5 to 8.0, depending on the counteranion of the salt and the ambient humidity of the laboratory. The LiX/$C_{12}E_{10}$/H_2O LLC mesophases lose water at lower humidity levels and absorb water at higher humidity levels. The LiCl-containing mesophase holds as few as four structural water molecules per LiCl, whereas the $LiNO_3$ mesophase holds 1.5 waters per salt (least among those assessed). This ratio strongly depends on the atmospheric humidity level; the water/LiX mole ratio increases by 0.08 ± 0.01 H_2O in the LLC mesophases per percent humidity unit. Surprisingly, the LLC mesophases are stable (no salt leaching) in broad humidity (10−85%) and salt/surfactant mole ratio (2−10 LiX/$C_{12}E_{10}$) ranges. Attenuated total reflectance Fourier transform infrared spectroscopic data show that the water molecules in the mesophase interact with salt species more strongly in the LiCl mesophase and more weakly in the case of the nitrate ion, which is evident by the shift of the O−H stretching band of water. The O−H stretching peak position in the mesophases decreases in the order $\nu_{LiCl} > \nu_{LiBr} > \nu_{LiSCN} > \nu_{LiNO_3}$ and accords well with the H_2O/LiX mole ratio. The conductivity of the LLC mesophase also responds to the amount of water as well as the nature of the counteranion (X^-). The conductivity decreases in the order $\sigma_{LiCl} > \sigma_{LiBr} > \sigma_{LiNO_3} > \sigma_{LiSCN}$ at low salt mole ratios and in the order $\sigma_{LiBr} > \sigma_{LiCl} > \sigma_{LiNO_3} > \sigma_{LiSCN}$ at higher ratios due to structural changes in the mesophase.

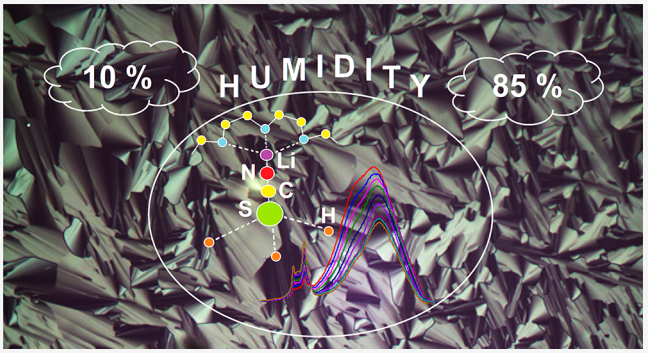

INTRODUCTION

Electrochemical cells, consisting of three major components, an anode, a cathode, and an electrolyte, are widely employed to store and convert clean and renewable energy.[1] Electrolytes are important components of these cells because the ion transport and electrode contacts occur within and with the electrolyte.[2] For these applications, electrolytes must have good ion conductivity, large electrochemical windows, low toxicity, low volatility, low flammability, and high viscosity.[3] Most of the organic-based and water-based electrolytes fail in one or more of these realms.[4] Gel electrolytes could be a good alternative to solution-based electrolytes if their conductivity issues could be resolved.[5−12] Liquid crystalline electrolytes (LCEs) have also been widely investigated in the literature as gel electrolytes.[8−24] The liquid crystalline gel electrolytes are in general in two different forms, thermotropic[12] and lyotropic liquid crystalline (LLC),[17−19] such as salt/surfactant LLC mesophases.[20−22] LCEs have been employed as gel electrolytes in many ways[15−24] such as optical modulation of graphene, effectively switching electrochromic devices, and dye-sensitized solar cells.

Salt/surfactant mesophases make up an important class of materials that could be used as gel electrolytes in electrochemical systems and constitute an important platform[20−22] for the synthesis of mesoporous materials.[25−28] Salts in their molten state or as a highly saturated solution can organize surfactants into liquid crystalline phases.[20,29−31] In the salt/surfactant LLC mesophases, molten salt or saturated salt solutions act as a nonvolatile solvent as one of the major components of the phase. Therefore, the salt/surfactant LLC mesophase differs from the salt-containing and salt free water/surfactant LLC mesophase[32−35] in terms of phase stability and usability in material synthesis and design.[25−28] Moreover, one

Received: September 12, 2021
Revised: November 22, 2021
Published: December 3, 2021

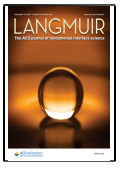

https://doi.org/10.1021/acs.langmuir.1c02411
Langmuir 2021, 37, 14443−14453

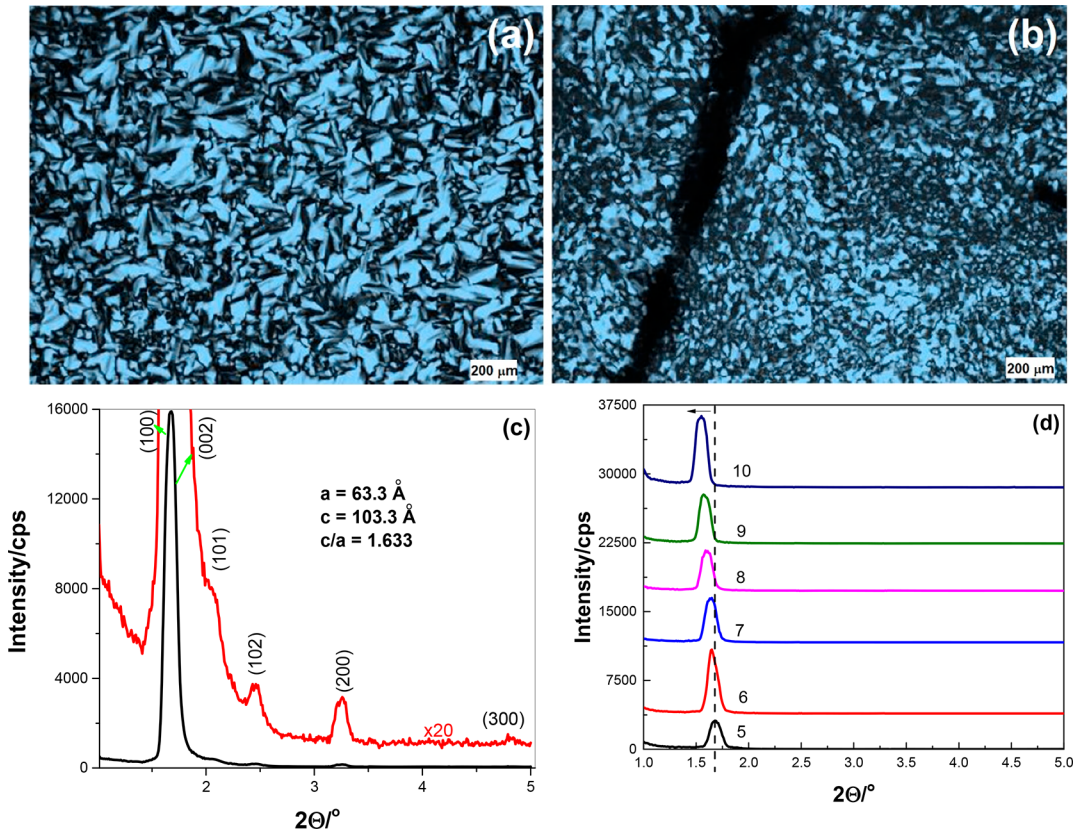

Figure 1. POM images of (a) $2LiCl/C_{12}E_{10}/H_2O$ and (b) $3LiBr/C_{12}E_{10}/H_2O$ systems and small angle XRD patterns of (c) $4LiCl/C_{12}E_{10}/H_2O$ (red line, magnified 20 times) and (d) $5-10LiBr/C_{12}E_{10}/H_2O$ (aged for 8 months) systems.

can also use a volatile solvent in addition to the salt/surfactant mixture to obtain homogeneous solutions. The solutions spread over any substrate to afford the salt/surfactant mesophase as thin films.[25−28] Thinner gel films can be prepared by simply diluting the solution or spin coating solutions at a higher speed. The LLC film can be as thin as tens of nanometres as determined by this approach. This gives flexibility and applicability to the LLC phases. Another important aspect in such a self-assembly process is the amount of water in the mesophase. The amount of water determines the structure, stability, and conductivity of these mesophases. Therefore, investigating the role of water and understanding the specific effects of ions on water are important for the development of water-based LLC gel electrolytes.

Specific ion effects were first reported by Hofmeister in 1888 for the separation of proteins.[36,37] Although substantial effort has been focused on exploring the underlying mechanisms of the reoccurring ion series, there is still no unified theory to explain the role of ions in colloidal and molecular assembly systems in various aqueous media.[38−42] The Hofmeister series ($CO_3^{2-} > SO_4^{2-} > S_2O_3^{2-} > HPO_4^{2-} > H_2PO_4^- > F^- > CH_3COO^- > Cl^- > Br^- > NO_3^- > I^- > ClO_4^- > SCN^- > I_3^-$) has been expanded over the years, including many anions and cations using different macromolecules and colloids.[43−50] This work focuses on only the effect of anions. In this series, the anions on the left-hand side of the series are kosmotropic and enhance the structure of water (also termed structure makers) and the other end is chaotropic and breaks the structure of water (structure breakers) and interacts with the macromolecules via direct binding or through their hydration water molecules.[43−50] Recent experimental results show that these behaviors dominate on the ion and its hydration shell(s), yet there is no probe for exploring the bulk water structure. The literature data were obtained by probing the local O−H stretching or bending modes by surface selective techniques such as vibrational sum frequency generation and their dynamics explored by two-dimensional (2D) infrared (IR) spectroscopy.[51−54]

Here, we examine $LiX/C_{12}E_{1O}$ LLC systems {where X is Cl^-, Br^-, NO_3^-, or SCN^- and $C_{12}E_{1O}$ refers to $[C_{12}H_{25}(OCH_2CH_2)_{10}OH]$} that could be employed to explore the function of water and its interaction with ions and surfactant domains using gravimetric, spectroscopic, and conductivity measurements. Evaporation from the salt/surfactant solutions, prepared in excess water, is monitored over time until the gel phase forms as determined by gravimetric, spectroscopic, and conductivity techniques. Notice that at the end of this process, the LLC mesophase reaches an equilibrium with the surrounding water (atmospheric water) and contains the hydration water that is identified by spectroscopic (ATR-FTIR) and gravimetric techniques. These LLC mesophases display high ion conductivity with the potential to serve as an electrolyte for electrochemical cells. The LLC mesophase can also serve as a model system for exploring the specific effects of ions under water-starved conditions.

EXPERIMENTAL SECTION

Materials. All chemicals used in this work were Sigma-Aldrich grade and used as received with purities of ≥99%. Deionized water was obtained from a Millipore Synergy 185 water purifier.

https://doi.org/10.1021/acs.langmuir.1c02411
Langmuir 2021, 37, 14443−14453

Preparation of the LiX/xH_2O/$C_{12}EO_{10}$ Solutions. Predetermined amounts of salt (LiCl, LiBr, $LiNO_3$, and LiSCN), surfactant [$C_{12}H_{25}(OCH_2CH_2)_{10}OH$ represented as $C_{12}E_{10}$], and 5 g of water are placed in a vial and stirred for ≥6 h to afford homogeneous solutions. Compositions of all of the LiCl, LiBr, $LiNO_3$, and LiSCN solutions used in this work are listed in Tables S1−S4, respectively.

Preparation of LiX/$C_{12}E_{10}$/H_2O LLC Mesophases. The solutions were coated over glass slides as films, and then the excess water was evaporated for 24 h under ambient laboratory conditions to afford the LLC mesophase.

Instrumentation. Polarized optical microscope (POM) images were recorded using a ZEISS Axio Scope A1 polarizing optical microscope. The X-ray diffraction patterns were recorded by using a Rigaku Miniflex diffractometer, having a high-power Cu Kα source operating at 30 kV and 15 mA with a wavelength of 1.5405 Å. The measurements were conducted by spreading the samples on clean glass slides by either spin-coating at different spin rates or drop casting. Small angle X-ray diffraction (XRD) patterns were collected from 1° to 5° and high-angle XRD patterns were collected from 5° to 60°, 2θ, with scan speeds of 0.5°/min and 5.0°/min, respectively. Attenuated total reflectance Fourier transform infrared (ATR-FTIR) spectra were recorded by using a Bruker Alpha-P FT-IR spectrometer with an ATR attachment. The spectra were recorded by dropping the samples on the ATR diamond and recording the spectra over time during the evaporation of water. The humidity-dependent spectra were also recorded by using a homemade setup, in which a saturated salt solution in a vial is placed next to the sample and sealed using a plastic container to adjust the humidity. Saturated solutions of LiCl, $MgCl_2$, K_2CO_3, NaBr, KI, NaCl, and KCl salt ensure 11%, 33%, 43%, 57%, 68%, 75%, and 85% humidity on the sample, respectively.[55] Ion conductivities of the samples were measured by employing ac impedance spectroscopy using a Gamry G750 potentiostat/galvanostat and a homemade conductivity cell.[19] First, a 0.01 M KCl standard solution, which has a conductivity of 1.413 mS/cm, is used to determine the cell constant (K) using the conductivity equation ($\sigma = K/R$, where σ is the conductivity in siemens per centimeter and R is the measured resistance in ohms) and measured resistance. Then, the same cell is cleaned and reused to measure the resistance of the sample solution at any time during the evaporation of water. The resistance data are converted to time-dependent conductivity by using the predetermined cell constant. The humidity-dependent conductivity data of the gel samples were collected by using the same saturated salt solutions in the vicinity of the conductivity cell in a sealed constant-volume chamber.

RESULTS AND DISCUSSION

Clear aqueous solutions of LiX (X is Cl^-, Br^-, I^-, NO_3^-, or SCN^-) and $C_{12}E_{10}$ in a broad range of salt amounts (LiX/$C_{12}E_{10}$ mole ratio of 2−10) were prepared as homogeneous solutions (all ingredients are fully dissolved, especially the surfactant molecules). As a first set of experiments, the solutions were coated over glass substrates for characterization by POM and XRD. Coating and then aging steps ensure the formation of an LLC mesophase. Figure 1 shows characteristic POM images and XRD patterns, recorded using various LiX/$C_{12}E_{10}$ mesophases. Careful inspection of the POM images together with XRD patterns shows that the LiX/$C_{12}E_{10}$ LLC mesophases have a 2D hexagonal structure (except LiSCN/$C_{12}E_{10}$) at low salt concentrations and display a focal conic fan texture (see Figure 1a). However, increasing the amount of LiX in the mesophase (such as 4LiCl/$C_{12}E_{10}$/4$m$$H_2O$, where m is the H_2O/LiCl mole ratio, and 3LiBr/$C_{12}E_{10}$/3$x$$H_2O$, where x is the LiBr/$C_{12}E_{10}$ mole ratio) leads to a change in the texture (see Figure 1b) that is characteristic of a three-dimensional (3D) hexagonal mesophase.[52] The XRD patterns of these samples are also in accord with this transformation (2D to 3D hexagonal); the diffraction lines [such as (002), (101) and (102)] that do not exist in the 2D hexagonal phases appear in the patterns (see Figure 1c).[56,57] With a further increase in the molar ratio of LiBr to >5, in the LiBr/$C_{12}E_{10}$/H_2O LLC, the mesophase becomes cubic and dark under the POM. However, LiCl and $LiNO_3$ mesophases are hexagonal in all compositions, at LiX/$C_{12}E_{10}$ mole ratios from 2 to 10. Figure 2 schematically summarizes the phase behavior of LiX/

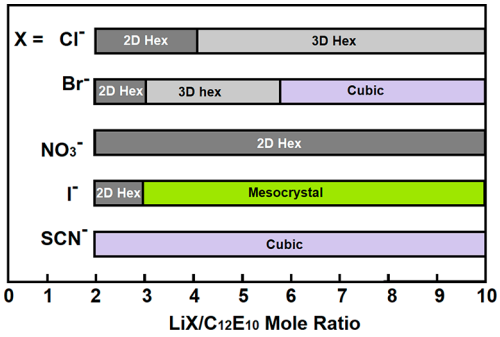

Figure 2. Diagram summarizing the phase behavior of the LiX/$C_{12}E_{10}$/H_2O mesophases.

$C_{12}E_{10}$/H_2O LLC mesophases. Notice that the morphology of the LLC mesophase changes with counteranion (see Figure 2). It is due to the amount of water each ion holds in the mesophase and the change in the ion−water−surfactant interactions (see below). Figure 1d displays a set of diffraction patterns recorded from LiBr/$C_{12}E_{10}$/H_2O mesophases. The gradual shift of the main line to smaller angles indicates that increasing the amount of LiBr in the mesophase also increases the unit cell dimensions that gradually expand to accommodate extra salt/water species in the hydrophilic domains of the mesophase; the typical expansion is ∼25% in the 10LiBr/$C_{12}E_{10}$ mesophase (see Figure 1d). The phase transformation, from 2D (disordered along the c-axis, cylindrical micelle surfactant domains) to 3D hexagonal (spherical micelle surfactant domains) and to the cubic phase with an increase in salt content, occurs for the same reason; simply, the mesophase expands its hydrophilic domains to accommodate more LiX/H_2O species. A similar trend is observed in the LiI/$C_{12}E_{10}$ mesophase that is 2D hexagonal at low salt concentrations, but the LLC phase transforms into a soft mesocrystal at mole ratios of >3.[58] Moreover, the LiI/$C_{12}E_{10}$ mesophase has been previously investigated in the presence of I_2 as a gel electrolyte in dye-sensitized solar cells.[59] Therefore, we excluded the LiI/$C_{12}E_{10}$/H_2O system and did not investigate it further in this work. The patterns in Figure S1 show the XRD patterns of the LiSCN/$C_{12}E_{10}$/H_2O system at small and large angles. Because the mesophases are dark under POM, it is reasonable to suggest that the LiSCN/$C_{12}E_{10}$/H_2O system is cubic at all concentrations. Keeping these basic characterizations in mind, we have investigated each system further to evaluate the amounts of water and its behavior in each LLC system by monitoring the evaporation of water under various conditions using gravimetric, spectroscopic, and conductivity techniques.

First, the LiX/$C_{12}E_{10}$ solutions were prepared in 5 mL of water. Then, a small amount of each solution was dropped over a balance, and its evaporation of water was gravimetrically monitored for 24 h. Figures 3a shows the weight change of the sample over time for the LiCl system with a LiCl/$C_{12}E_{10}$ mole ratio of 5 (the other mole ratios and salt systems are given in

https://doi.org/10.1021/acs.langmuir.1c02411
Langmuir 2021, 37, 14443−14453

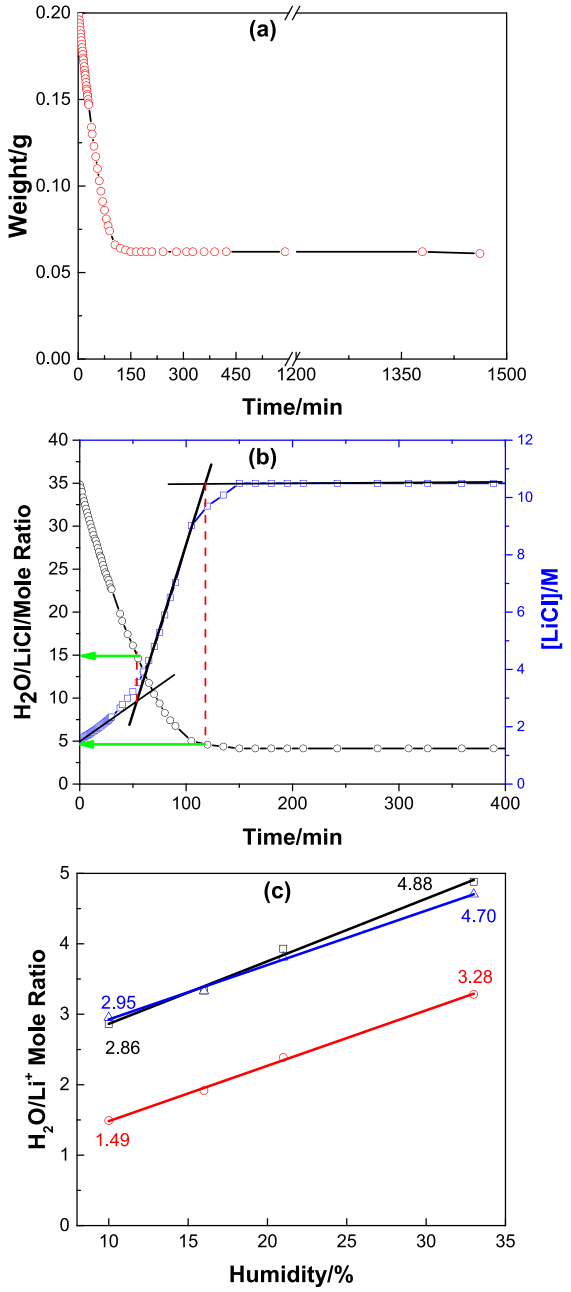

Figure 3. Evaporation of water. (a) Gravimetric data of the 5LiCl/$C_{12}E_{10}$/H_2O system (28% humidity). (b) H_2O/LiCl mole ratio and [LiCl] vs time (guide to the eyes) of the 5LiCl/$C_{12}E_{10}$/H_2O system. (c) Humidity-dependent H_2O/LiX mole ratio of the LLC phases of 5LiX/$C_{12}E_{10}$/H_2O samples (fitted to a linear equation; blue for LiCl, black for LiBr, and red for $LiNO_3$).

the Supporting Information; see Figures S2−S4). The weight versus time plot drops perfectly linearly and reaches a plateau, where the change stops after 24 h. Because the initial composition of the solution is known and assuming the salt and surfactant do not evaporate and remain unchanged over time, the weight change can be directly attributed to lost water. Therefore, the sum of the weight of salt and surfactant (W_{ss}) is known in the initial solution and remains constant during the evaporation of water. The final weight (W_f) of the sample minus the sum of the salt and surfactant weight of the solution ($W_f - W_{ss}$) is the weight of water (W_w) that remains in the mesophase. The amount of water in the sample at time t (W_{wt}) can also be calculated by simply subtracting W_{ss} from the weight of the sample (W_s) at the same time t ($W_{wt} = W_s - W_{ss}$). Therefore, the H_2O/LiX mole ratio can also be calculated at any time (see the plot in Figure 3b). The straight black lines on the plots in Figure 3b and Figures S2−S4 clearly show three regions of evaporation of water with different kinetics. Table 1 shows the calculated H_2O/LiX mole ratios of all compositions for all salt/surfactant systems, upon complete evaporation of water. We also evaluated the change in the salt concentration ([LiX], calculated using only LiX and water) during evaporation of water and plotted the data together with the H_2O/LiX mole ratio versus time. The plot of $[LiX]_t$ versus time displays at least three main regions, where the evaporation of water follows different kinetics. In the first region or step, the change in [LiX] is slow. We assume this is the evaporation of only bulk water; the mixture is still in the liquid phase in this region. In the second region or step, the change is faster and corresponds to a gelation (macroscopically, the liquid mixture transforms into an LLC gel), and in the third region, there is further yet slow evaporation of water from the LLC gel phase. The break points between the regions in the plot also provide valuable information and serve as reference points with regard to evaporation of water, gelation, and stability of the LLC phases. For instance, in the 5LiCl/$C_{12}E_{10}$ sample, the gelation process starts around 15H_2O/LiCl and reaches completion around 5H_2O/LiCl. However, evaporation of water continues in the gel phase and reaches equilibrium around 4H_2O/LiCl.

From these measurements and calculations, we found that as the LiX concentration increases in the mesophase, the H_2O/LiX mole ratio remains almost constant. However, for the salts of more chaotropic anions, such as LiSCN, the H_2O/LiSCN mole ratio remains constant at around 1.9 for samples with a LiSCN/$C_{12}E_{10}$ mole ratio of ≤5. However, it gradually increases with a further increase in the amount of LiSCN in the mesophase and reaches 2.7 for samples with a LiSCN/$C_{12}E_{10}$ mole ratio of 10. However, all H_2O/LiX mole ratios are subject to the humidity level of the laboratory. It increases linearly with humidity. This is also clear in the plots in Figure 3c. The third region of the evaporation of water corresponds to the gel phase that is stable over a broad range of water contents. This range corresponds to the humidity tolerance region in a stable gel phase. Therefore, we also identified the H_2O/LiX mole ratios at different humidities. The humidity levels of the samples were set by keeping the samples in a humidity chamber or in a closed container together with a saturated salt solution that provides a constant humidity at a given temperature.

The humidity-dependent H_2O/LiX mole ratios were evaluated using 5LiX/$C_{12}E_{10}$ samples of all four salts. Notice also that the H_2O/LiX mole ratio varies from day to day due to the change in the humidity of our laboratory (see Table 1). We picked four different days with four different humidity levels of 10%, 16%, 21%, and 33%. The plot in Figure 3c shows that there are slight differences from salt to salt, but the change in the H_2O/LiX mole ratio fits a linear function with an R^2 of ≥0.99. The slope of the plots varies from 0.08 ± 0.01H_2O/LiX mole ratio per humidity. In fact, this is not a small amount of water in the mesophase; for instance, in the $LiNO_3$ sample, the change, from 10% to 33% humidity, is from 1.49H_2O/$LiNO_3$ to 3.28H_2O/$LiNO_3$ (it is 2.2 times or an increase from 7.5 to 16.4 in the H_2O/$C_{12}E_{10}$ mole ratio). It is similar in LiCl and LiBr samples, in which the amount of water increases by 1.7 and 1.6 times, respectively. Therefore, the fluctuation of the

https://doi.org/10.1021/acs.langmuir.1c02411
Langmuir 2021, 37, 14443−14453

Table 1. H_2O/LiX Mole Ratios in the nLiX/$C_{12}E_{10}$/$m$$H_2O$ LLC Mesophase (X^- is Cl^-, Br, NO_3^-, or SCN^-, and m is n times the H_2O/LiX mole ratio), Calculated from Gravimetry Data

	LiCl		LiBr		$LiNO_3$		LiSCN	
Salt/$C_{12}E_{10}$ ratio (n)	1 day	4 days	1 day	4 days	1 day	4 days	1 day	4 days
1.3	–	–	–	–	–	–	2.1	1.7
2	4.49	3.63	3.69	2.73	1.99	1.58	2.0[a]	1.6[a]
3	3.69	5.75	3.68	3.10	1.52	1.32	2.0[b]	1.5[b]
4	4.11	3.17	3.49	2.78	1.99	1.45	1.9	1.6
5	4.40	3.84	4.25	3.97	2.37	2.04	2.0	1.9
6	3.08	3.81	5.23	6.27	1.89	2.08	2.2	2.1
7	3.96	3.91	3.74	3.90	2.08	2.05	2.3	2.2
8	4.02	3.84	4.03	3.93	2.40	2.05	2.4	2.4
9	4.52	4.08	4.43	3.98	1.42	2.05	2.6	2.5
10	4.32	3.83	4.33	4.27	2.38	2.19	2.7	2.5

[a]LiSCN/$C_{12}E_{10}$ mole ratio of 1.9. [b]LiSCN/$C_{12}E_{10}$ mole ratio of 2.

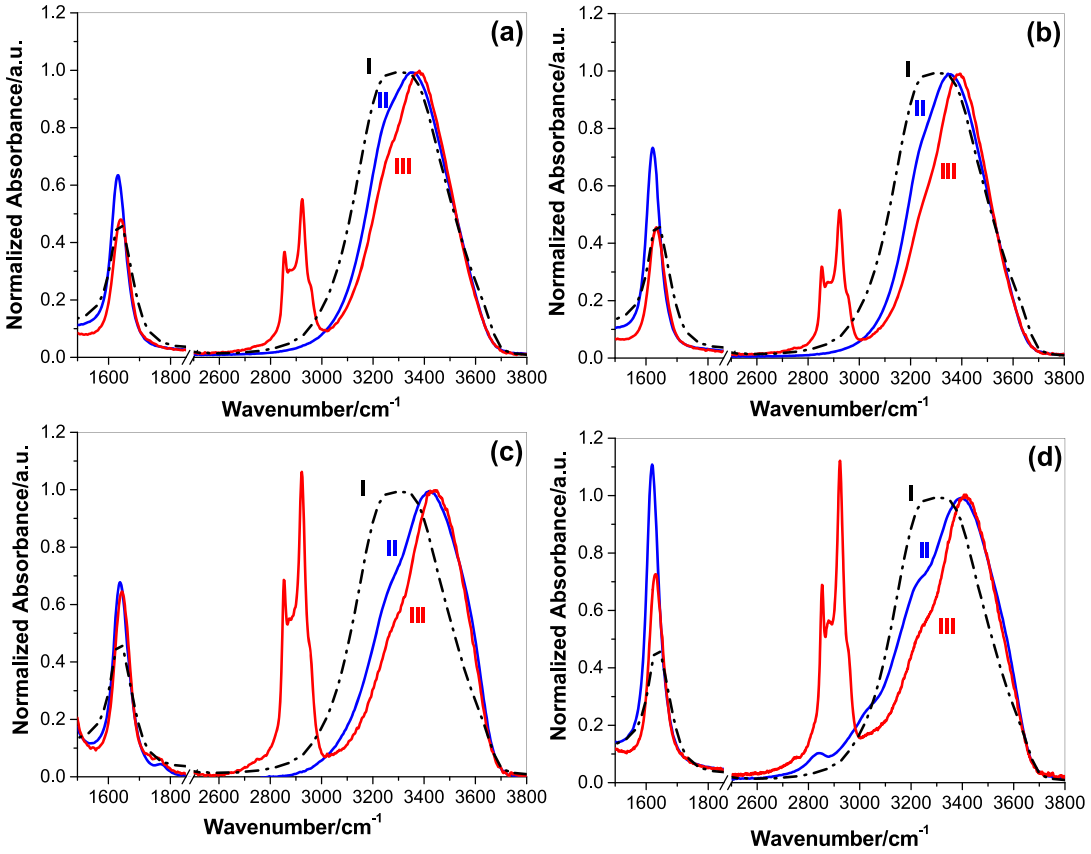

Figure 4. ATR-FTIR spectra of (I) H_2O, (II) a saturated LiX solution, and (III) a 5/1 LiX/$C_{12}E_{10}$ mole ratio gel, where X is (a) Cl^-, (b) Br^-, (c) NO_3^-, or (d) SCN^-.

H_2O/LiX mole ratios in Table 1 is due to the mildly changing humidity level of the laboratory.

In another set of experiments, we employed ATR-FTIR spectroscopy to investigate the spectral changes and water removal process in the LiX/$C_{12}E_{10}$/H_2O systems. In Figure 4, the water bending and stretching spectral regions are plotted in four panels for the samples containing LiCl, LiBr, $LiNO_3$, and LiSCN as saturated aqueous solutions and as LLC mesophases together with neat water. It was clear for all spectra that as the relative salt concentration increases the intensity of the water spectra decreases primarily from its ice-like (tetrahedral H-bonded) water signal around 3200 cm^{-1}. Moreover, the band due to more weakly interacting water (water-like) assigned to around 3400 cm^{-1} blue-shifts. When we move from the saturated salt solutions to gel LLC mesophases of these salts, the effect of the salt on water is clearly enhanced. Namely, the intensity of the 3200 cm^{-1} band decreases further and the water stretching band blue-shifts even further. The blue-shift in the O−H stretching band is generally attributed to weaker H-bonds in aqueous solutions and interfacial water molecules.[54] It was also shown that weaker H-bonds should yield a red-shift in the H−O−H bending mode.[54,60,61] In sharp contrast in the LLC mesophase, it is difficult to form a direct analogy to known aqueous phase systems simply due to very small water/salt mole ratios formed by the stable LLC mesophases (as low as 2). As such, the major contribution to the spectral changes

https://doi.org/10.1021/acs.langmuir.1c02411
Langmuir 2021, 37, 14443−14453

here should be the lack of the H-bonding network of water (partially eliminated intermolecular coupling) as well as structural water, trapped between the ions and surfactants, and in the hydrations. These water spectra clearly indicate that the LLC phase contains salt/water mixtures, which has an even higher salt ion concentration, and thus, it contains water molecules that are more distorted compared to saturated salt solutions.

Moreover, ATR-FTIR spectroscopy can also be applied to monitor the entire water removal process. A drop of the sample solution with known initial compositions was placed on the ATR diamond crystal, and the spectra were recorded as a function of time. Figures S5–S9 show a set of row spectra of the 5LiX/$C_{12}E_{10}$/H_2O system during evaporation of water and a set of normalized spectra of the 5LiBr/$C_{12}E_{10}$/H_2O system. One must be careful how to evaluate this set of data to understand the observed changes (see the Supporting Information under ATR-FTIR). Comparing the raw ATR-FTIR spectra of a sample, which undergoes multiple changes over time by changing its concentration and/or refractive index, can be misleading. This work is an excellent example for such samples (increases in both concentration and refractive index). Therefore, we normalized the time-dependent data using surfactant signals, the (ν_{as}-CH_2) peak at 2923 cm^{-1}. Namely, we used the surfactant as an internal reference in the sample and report our results per surfactant (see the Supporting Information for details). Because the gel has the highest refractive index and concentration, it has the highest absorbance. The spectrum of the gel, recorded after the complete evaporation of water, is used to evaluate the normalization constants of each spectrum recorded during the evaporation of water. In other words, the time-dependent spectra are normalized to the spectrum of the sample after the evaporation of water reaches an equilibrium. The typical normalization constant of the first spectrum is around 6–8. The intensity of the normalized water peak decreases from 2.25 to 0.21 absorbance unit (see Figure S9). The intensity ratio is ~10.5 and consistent with the gravimetric data. Note that the H_2O/LiBr mole ratio is ~35.2 in the initial solution and decreases to 3–5 after the evaporationof water for 24 h, depending on the percent humidity level of the laboratory for the 5LiBr sample.

Figure 5 shows the difference spectra, obtained from the normalized spectra, and displays the time-dependent spectral changes [in three different time domains during the evaporation of water from the LiCl/$C_{12}E_{10}$/H_2O (5/1/176) sample, like gravimetric data]. In the first region, the spectral changes show the evaporation of bulk water. This is evident because the spectral shape in this region is quite like that of bulk water. The spectral changes in the water stretching region change in the second region, indicating a change in the type of water evaporating from the sample, and correspond to evaporation of bulk and water in the extended hydration shells (except the first hydration shell due to energy considerations). In the third region, the spectral changes correspond to evaporation of hydration water. All three peak maxima due to water stretching, bending, and libration modes blue-shift from one region to the next (see Figure 5). As the O–H bond strengthens, the stretching bands blue-shift and the strength of hydrogen bonding becomes weaker among the hydration water molecules in the mesophase. All other LiX/$C_{12}E_{10}$/H_2O (X is Cl^-, Br^-, NO_3^-, and SCN^-) samples, at LiX/$C_{12}E_{10}$ mole ratios from 2 to 10, were also followed

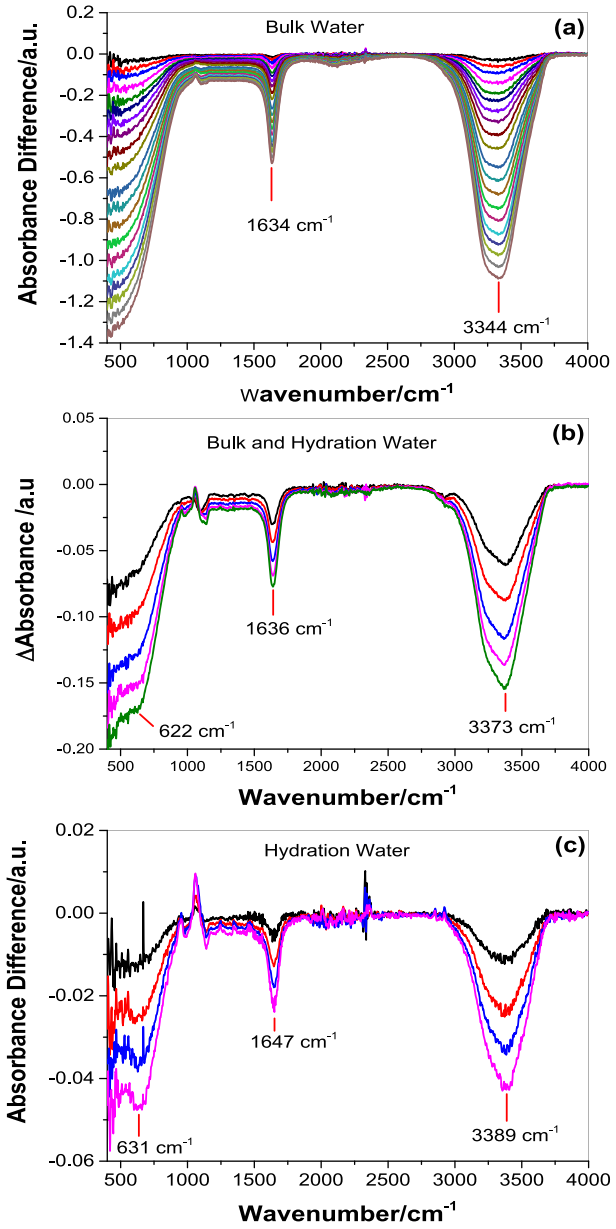

Figure 5. Difference spectra of the normalized ATR-FTIR spectra, recorded during the evaporation of water from the 5LiCl/$C_{12}E_{10}$/H_2O system (a) from a solution, (b) during gelation, and (c) from a gel.

spectroscopically (see Figures S10–S12), and similar trends were observed consisting of the same three regions.

Figure 6a shows the ATR-FTIR spectra of the LiSCN/$C_{12}E_{10}$/H_2O system at different LiSCN/$C_{12}EO_{10}$ mole ratios. As gravimetrically determined in the LiSCN samples, the H_2O/LiSCN ratio gradually increases above 5LiSCN/$C_{12}E_{10}$ mole ratio samples. Because of the surfactant (ν_{as}-CH_2) peak at 2923 cm^{-1}, used as a reference for normalization of the spectra, the intensity of water peak maxima (I_W) can be divided by the surfactant peak intensity (I_S) to normalize the spectra of each LiX sample at different mole ratios. Figure 6b shows the plots of I_W/I_S versus LiX/$C_{12}E_{10}$ mole ratios. Each plot fits a linear relationship (R^2 varies from 0.95 to 0.99) with a different slope; the values are 0.41, 0.40, 0.27, and 0.17 for LiCl, LiBr, LiSCN, and $LiNO_3$, respectively (see Figure 6). This trend is consistent with the gravimetric data.

https://doi.org/10.1021/acs.langmuir.1c02411
Langmuir 2021, 37, 14443–14453

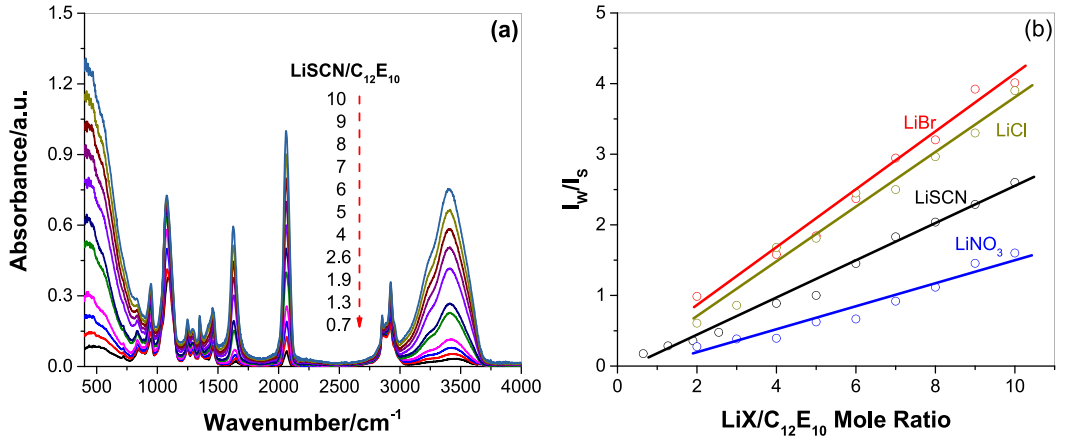

Figure 6. (a) ATR-FTIR spectra of LiSCN/$C_{12}E_{10}$/H_2O mesophases at LiSCN/$C_{12}E_{10}$ mole ratios from 1.3 to 10 and (b) plot of I_W/I_S vs LiX/$C_{12}E_{10}$ mole ratio (fits to a linear equation) of all LLC phases.

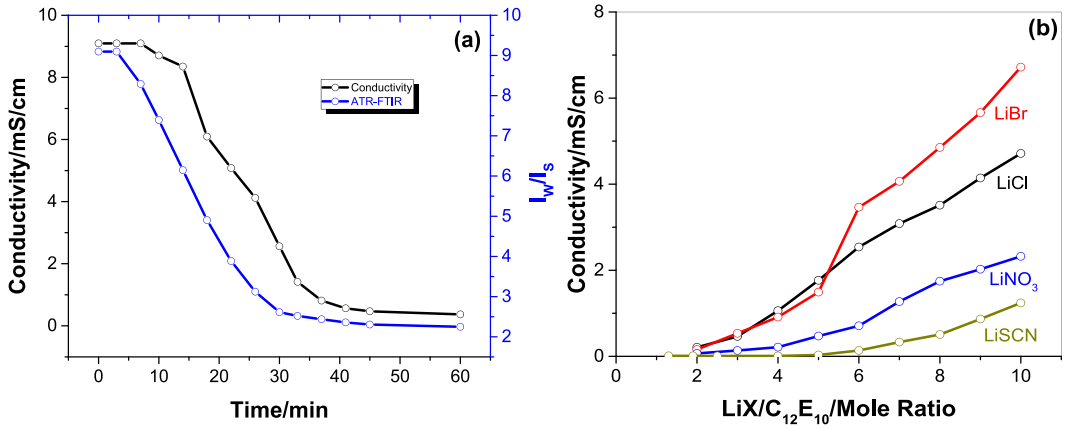

Figure 7. (a) Plots of conductivity vs time and I_W/I_S ratio vs time of the 5LiBr sample and (b) plots of conductivity vs LiX/$C_{12}E_{10}$ mole ratio of LiX/$C_{12}E_{10}$/H_2O mesophases [X is Cl^- (black), Br^- (red), NO_3^- (blue), and SCN^- (dark yellow)]. Symbols show data points, and lines only connect the data points.

The evaporation of water was also monitored using conductivity measurements. The conductivity was measured using a homemade cell using FTO glass (see the Experimental Section for details). The plot of conductivity versus time closely follows the I_W/I_S in the ATR-FTIR spectroscopic data (see Figure 7a). The conductivity plot can also be divided into three regions, solution phase, gelation, and evaporation of excess water in the gel phase. The conductivity slowly decays as water evaporates from the solution phase (see Figure 7a). This is consistent with the formation of ion pairs and the decay in the mobility of free ions in the solution with an increase in the viscosity of the media together with mesophase formation. The decrease in conductivity is sharper during gelation and further decreases in the gel phase. Figure 7b shows the variation in conductivity with an increase in the level of LiX in the LiX/$C_{12}E_{10}$/H_2O mesophases. It is also important to notice that the amount of water in the mesophase is more dominant in the conductivity values. With complete evaporation of water under a constant humidity, the conductivity gradually increases with an increasing salt/surfactant ratio in the following order: $\sigma_{LiCl} > \sigma_{LiBr} > \sigma_{LiNO_3} > \sigma_{LiSCN}$. However, the order changes at a salt/surfactant ratio of 5: $\sigma_{LiBr} > \sigma_{LiCl} > \sigma_{LiNO_3} > \sigma_{LiSCN}$. There is a sharp increase in the conductivity of 6LiBr, due to a change in the mesostructure. Indeed, the LiBr/$C_{12}E_{10}$/H_2O mesophase transforms from hexagonal to cubic at around the same mole ratio. A similar behavior exists in other LLC phases in which the phase transformation from hexagonal to cubic enhances the conductivity.[62]

The ATR-FTIR technique was also employed to check the response of the humidity of the samples using a homemade setup that provides a constant humidity using saturated salt solutions. A drop of the LiX/$C_{12}E_{10}$/H_2O solution was placed over the ATR crystal and aged for gelation (until it reaches an equilibrium, aged for 24 h); then the saturated salt solution was placed next to the sample in a vial, and the sample and saturated salt solution together were sealed with a plastic container to ensure a well-sealed atmosphere with a constant volume. Then, the spectrum of the sample was recorded after it had aged for an additional 24 h to ensure the sample reaches a new equilibrium under the new humidity conditions. This test was repeated using the atmosphere of each saturated solution (LiCl, $MgCl_2$, K_2CO_3, NaBr, KI, NaCl, and KCl salts that ensure 11%, 33%, 43%, 57%, 68%, 75%, and 85% humidity, respectively). Figure 8a shows the water stretching region of the normalized ATR-FTIR spectra of the 5LiCl sample. The inset of Figure 8a is the plot of I_W/I_S that follows a linear dependence and only positively deviates at low humidity. However, the amount of water in the sample gradually increases by 3 times going from 11% to 85% humidity. The same sample was checked to determine whether the

https://doi.org/10.1021/acs.langmuir.1c02411
Langmuir 2021, 37, 14443−14453

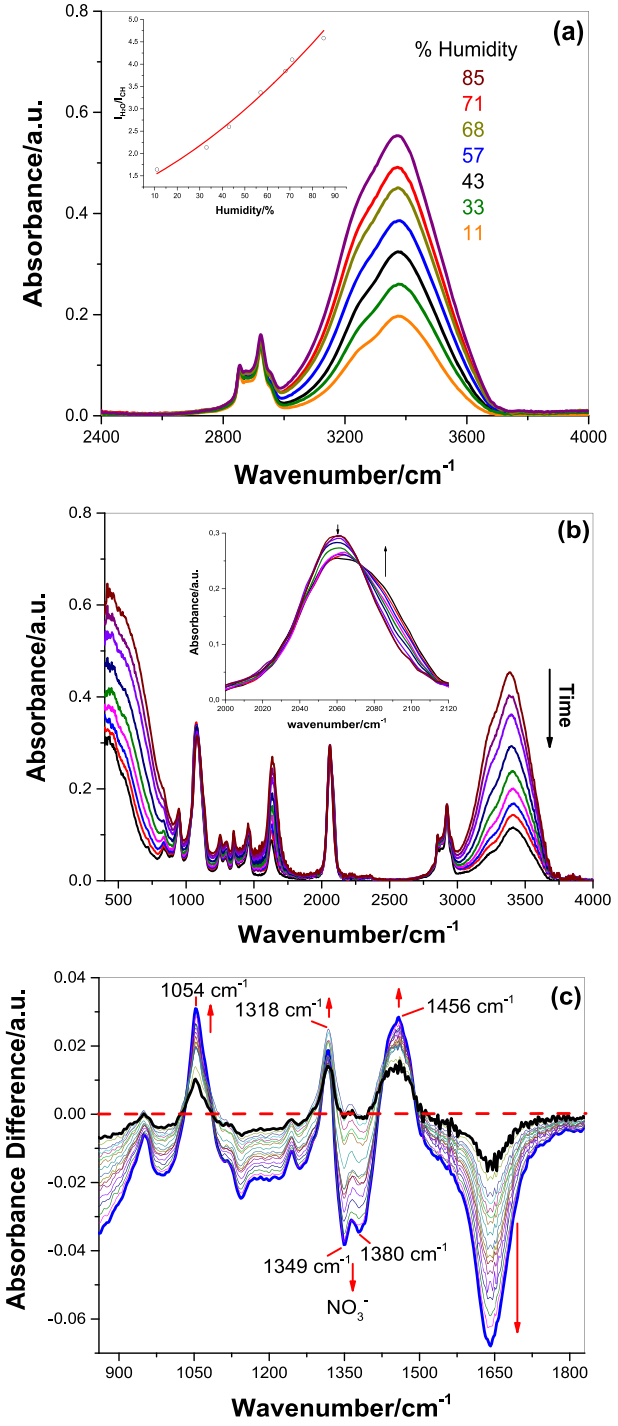

Figure 8. ATR-FTIR spectra of (a) the 5LiCl/$C_{12}E_{10}$/H_2O mesophase at various percent humidities (the inset is the plot of I_W/I_S vs humidity, fitted to an exponential function), (b) the third region of the 5LiSCN/$C_{12}E_{10}$/H_2O system (5−24 h period of evaporation of water; the inset is the ν-CN region), and (c) difference spectra in the third region of the 5$LiNO_3$/$C_{12}E_{10}$/H_2O system.

mesophase is still stable or not with such large amounts of water by keeping it in a humidity chamber, prior to gelation, at 75% humidity for 24 h. Then it is sealed in the humidity chamber with a cover glass to keep the water in the sample for inspection under POM. The POM image displays birefringent texture, indicating that the mesophase is still stable under such high humidity (see Figure S13). The humidity-dependent conductivity measurements were also carried at three different humidity levels using the same setup, and as expected, the conductivity gradually increases with the humidity of the atmosphere (see Table S5).

The time-dependent spectroscopic data (during the evaporation of water) were recorded for all salt systems and all compositions. Figure 8b shows a set of spectra collected from the 5LiSCN sample after it had aged for 5 h over the ATR crystal until 24 h. The I_W/I_S ratio decreases from 11.94 to 3.44 in the first 5 h and further decreases to 0.87 in 24 h. After the sample had been aged for 24 h, its composition was 5/1/10 LiSCN/$C_{12}E_{10}$/H_2O, with two waters per LiSCN. Note also that the spectra display features similar to those recorded under around 75% to 17% humidity, at which the LLC gel phase is stable. This region also corresponds to the third region in the gravimetric data. The inset of Figure 8b shows the ν-CN stretching region of the same spectra. Notice that the ν-CN region is observed around 2060 cm^{-1}, but at such a high salt concentration, the SCN^- ions cannot remain as free ions; it instead forms ion pairs (Li-SCN) and dimers [$Li_2(SCN)_2$], which appear at 2081 and 2045 cm^{-1}, respectively, in the spectrum.[63,64] Clearly, different ionic species (free ion, ion pair, and dimer) coexist in the mesophase even in the solution phase. With the evaporation of water, specifically in the third region, the intensity of the ion-pair band (at ∼2081 cm^{-1}) gradually increases at the expense of that of the free ion (∼2060 cm^{-1}) (see the inset of Figure 8b). Unlike the spectra of LiBr/$C_{12}E_{10}$/H_2O and LiCl/$C_{12}E_{10}$/H_2O samples, the spectra of both LiSCN/$C_{12}E_{10}$/H_2O and $LiNO_3$/$C_{12}E_{10}$/H_2O samples display features related to SCN^- and NO_3^- ions, respectively. Like SCN^- ions, the NO_3^- ions also display features related to the ion pair and dimers. The free nitrate ion appears at 1350 cm^{-1} as a single peak due to doubly degenerate asymmetric stretching modes (ν_{as}-NO_3) in a dilute solution phase. However, even in the solution phase of our samples, the ν_{as}-NO_3 mode weakly splits into two due to strong and weak interaction with water;[65] however, with further evaporation of water, the splitting becomes large, indicating stronger interactions with the Li^+ ion as an ion pair and dimer. Figure 8c displays difference spectra toward the end of the evaporation of water (third region). The intensities of the ion-pair and dimer-related peaks, observed at 1318 and 1456 cm^{-1}, respectively, increase, and the peak intensity of the free nitrate, interacting with water, declines upon further evaporation of water in the 5$LiNO_3$/$C_{12}E_{10}$/H_2O mesophase, like in the case of SCN^- ions. The inactive symmetric stretching mode of the nitrate ion also appears as a peak around 1054 cm^{-1} due to the interactions mentioned above (see Figure 8c). The other features around 1100 cm^{-1} could be due to interaction, and a red-shift of the C−O-related peaks of the surfactant indicates that the $LiNO_3$ species are also interacting with the ethylene oxide sides of surfactant domains in the mesophase.

Overall, the ATR-FTIR spectroscopic data correlate with the gravimetry data. Figure 9 shows normalized ATR-FTIR spectra of all of the samples with LiX/$C_{12}E_{10}$ mole ratios of 5 after the evaporation of water and the stable mesophase form. As already determined from the gravimetric data, the amount of water kept in the mesophase decreases in the following order: LiCl > LiBr > LiSCN > $LiNO_3$. The water stretching peak maxima also follow the same trend; the peak maxima are observed at 3377, 3388, 3410, and 3444 cm^{-1}, respectively. The weakly H-bonded water molecules in the sample are

https://doi.org/10.1021/acs.langmuir.1c02411
Langmuir 2021, 37, 14443−14453

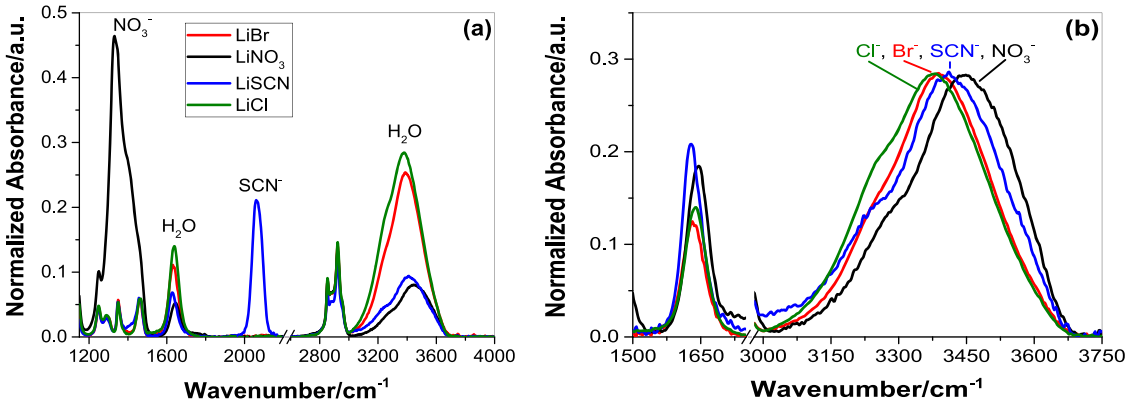

Figure 9. ATR-FTIR spectra of the $5LiX/C_{12}E_{10}/H_2O$ system (X is Cl^-, Br^-, SCN^-, or NO_3^-) after the complete evaporation of water (a) normalized to surfactant peaks and (b) normalized to the water peak.

present among the salt ions and between the ions and surfactant ethylene oxide domains. More importantly, the remaining water in the sample is the hydration water around the ions. For more weakly hydrated anions (SCN^- and NO_3^-), a small amount of water is necessary to maintain the stability of the mesophase. The required amount increases with monatomic anions. To gain more in-depth information, we also normalized all of the water stretching peak maxima (see Figure 9b) and compared the water bending modes. The bending region displays interesting behaviors. First, the frequency of the bending mode follows quite a different order, $\delta_{LiNO_3} > \delta_{LiCl} > \delta_{LiBr} > \delta_{LiSCN}$, with an intensity order of $I_{LiSCN} > I_{LiNO_3} > I_{LiCl} > I_{LiBr}$. The peak position and intensity orders together show that the molecular level picture is complex. Although the stretching band positions show H-bond weakening in the samples, the bending mode does not support this notion with the expected red-shifted peak positions. This should be due to the structurally broken H-bond network of water.

Surprisingly, the ion specific effects shown in this study do not exactly follow the anionic Hofmeister series. However, the intensity ratios of the water stretching to bending bands phenomenologically follow the Hofmeister series. The ratios are 1.37, 1.64, 2.03, and 2.33 for LiSCN, $LiNO_3$, LiBr, and LiCl, respectively. The concepts of "structure makers" and "structure breakers" have lost their impact for aqueous solutions. For the water-starved systems, as we have shown for the LLC mesophases, the specific ion effects still hold the traditional view of structure makers and breakers of the H-bond network.

CONCLUSION

Lithium salts (LiX) and oligo(ethylene oxide) type surfactants, namely 10 lauryl ether, form lyotropic liquid crystalline mesophases in the presence of water in a broad range of salt amounts ($LiX/C_{12}E_{10}$ mole ratios of 1.3−10). Here, four lithium salts (LiCl, LiBr, $LiNO_3$, and LiSCN) were used to investigate the role of water that is required for mesophase formation. Aqueous solutions of LiX and $C_{12}E_{10}$ lose their excess water to form their LLC mesophases. The amount of water that remains in the mesophase depends on the salt and humidity. Typically, the H_2O/LiX ratio is around 4 for LiCl and LiBr mesophases but as low as 2 for LiSCN and 1.5 for $LiNO_3$ at around 20% humidity; it increases with humidity by 0.08 H_2O per humidity. Mesophases are also stable in a broad range of humdities (10−85% humidity; values outside of this range are not measured in this work). Evaporation of water from these solutions can be monitored by gravimetric, spectroscopic, and conductivity techniques. All methods show that there are three different evaporation regions in which the kinetics of evaporation of water are different. In the first region, evaporation of bulk water is observed from a highly saturated solution phase. In the second region, evaporation leads to the formation of the LLC mesophase (gelation, evaporation of bulk water, and likely the extended hydration spheres), where the evaporation slows. The last region is the release of water from the LLC mesophase, which is the slowest step. Typically, evaporation reaches completion in 24 h. The same process can be followed using ATR-FTIR spectroscopy. However, the spectra must be normalized to follow time-dependent changes during the evaporation of water. Normalization can be performed by either using the intensity of the surfactant C−H stretching bands or taking the change in LiX concentration into account (for instance, in the 5LiCl sample, the LiCl concentration changes from 1.6 to 11 M). Both water stretching and bending modes sense the X^- ions in the mesophase and can be put into an order. The stretching frequecy order of the four salts is as follows: $\nu_{LiCl} < \nu_{LiBr} < \nu_{LiSCN} < \nu_{LiNO_3}$ (related to hydrogen-bonding and ion−water interaction). The bending mode frequency and intensity also respond to the X^- ion type. The frequecy decreases in the following order: $\delta_{LiNO_3} > \delta_{LiCl} > \delta_{LiBr} > \delta_{LiSCN}$. The intensity decreases in the following order: $I_{LiSCN} > I_{LiNO_3} > I_{LiCl} > I_{LiBr}$. The order of ionic conductivity of the mesophases is as follows at a $LiX/C_{12}E_{10}$ mole ratio of <6: $\sigma_{LiCl} > \sigma_{LiBr} > \sigma_{LiNO_3} > \sigma_{LiSCN}$. The order is as follows due to a structural change in the mesophase: $\sigma_{LiBr} > \sigma_{LiCl} > \sigma_{LiNO_3} > \sigma_{LiSCN}$. The $LiBr/C_{12}E_{10}/H_2O$ mesophase is cubic at $LiBr/C_{12}E_{10}$ mole ratios of ≥6. The conductivity data can also be correlated with the spectroscopic data, showing that this order is related to the formation of an ion pair and dimerization and ion−surfactant interactions.

The methods employed in this work are unique for exploring the role of water and ions in the structure, mesophase stability, and assembly of LLC mesophases. Further investigations in other systems, such as acid/surfactant and transition metal salt/surfactant mesophases, may be performed to contribute to the discussion of specific ion effects from concentrated systems that have not yet been investigated.

https://doi.org/10.1021/acs.langmuir.1c02411
Langmuir 2021, 37, 14443−14453

■ ASSOCIATED CONTENT

Supporting Information

The Supporting Information is available free of charge at https://pubs.acs.org/doi/10.1021/acs.langmuir.1c02411.

ATR-FTIR principles, tables of compositions, small angle XRD patterns of the $LiSCN/C_{12}E_{10}/H_2O$ system, additional gravimetric data for the $LiX/C_{12}E_{10}/H_2O$ systems (X is Br^-, NO_3^-, or SCN^-), time-dependent ATR-FTIR spectra of the $LiX/C_{12}E_{10}/H_2O$ systems (X is Cl^-, Br^-, NO_3^-, or SCN^-), normalized ATR-FTIR spectra of the $LiX/C_{12}E_{10}/H_2O$ systems (X is Cl^-, Br^-, NO_3^-, or SCN^-), and humidity-dependent POM images of the $LiNO_3/C_{12}E_{10}/H_2O$ system (PDF)

■ AUTHOR INFORMATION

Corresponding Author

Ömer Dag − *Department of Chemistry and UNAM-National Nanotechnology Research Center and Institute of Materials Science and Nanotechnology, Bilkent University, 06800 Ankara, Turkey;* orcid.org/0000-0002-1129-3246; Email: dag@fen.bilkent.edu.tr

Authors

Ezgi Yılmaz Topuzlu − *Department of Chemistry, Bilkent University, 06800 Ankara, Turkey*

Halil I. Okur − *Department of Chemistry and UNAM-National Nanotechnology Research Center and Institute of Materials Science and Nanotechnology, Bilkent University, 06800 Ankara, Turkey;* orcid.org/0000-0002-2492-1168

Burak Ulgut − *Department of Chemistry and UNAM-National Nanotechnology Research Center and Institute of Materials Science and Nanotechnology, Bilkent University, 06800 Ankara, Turkey;* orcid.org/0000-0002-4402-0033

Complete contact information is available at: https://pubs.acs.org/10.1021/acs.langmuir.1c02411

Notes

The authors declare no competing financial interest.

■ ACKNOWLEDGMENTS

The authors thank TÜBİTAK (under Project 118Z820) for the financial support of this work. Ö.D. is a member of the Science Academy, Istanbul, Turkey.

■ REFERENCES

(1) Chu, S.; Cui, Y.; Liu, N. The path towards sustainable energy. *Nat. Mater.* **2017**, *16*, 16−22.

(2) Xia, L.; Yu, L.; Hu, D.; Chen, G. Z. Electrolytes for electrochemical energy storage. *Mater. Chem. Front.* **2017**, *1*, 584−618.

(3) Zhong, C.; Deng, Y.; Hu, W.; Qiao, J.; Zhang, L.; Zhang, J. A review of electrolyte materials and compositions for electrochemical supercapacitors. *Chem. Soc. Rev.* **2015**, *44*, 7484−7539.

(4) Xu, K. Nonaqueous liquid electrolytes for lithium-based rechargeable batteries. *Chem. Rev.* **2004**, *104*, 4303−4418.

(5) Pan, L.; Yu, G.; Zhai, D.; Lee, H. R.; Zhao, W.; Liu, N.; Wang, H.; Tee, B. C.-K.; Shi, Y.; Cui, Y.; Bao, Z. Hierarchical nanostructured conducting polymer hydrogel with high electrochemical activity. *Proc. Natl. Acad. Sci. U. S. A.* **2012**, *109*, 9287−9292.

(6) Li, L.; Shi, Y.; Pan, L.; Shi, Y.; Yu, G. Rational design, and applications of conducting polymer hydrogels as electrochemical biosensors. *J. Mater. Chem. B* **2015**, *3*, 2920−2930.

(7) Zhao, Y.; Liu, B.; Pan, L.; Yu, G. 3D nanostructured conductive polymer hydrogels for high-performance electrochemical devices. *Energy Environ. Sci.* **2013**, *6*, 2856−2870.

(8) Ahmad, Z.; Hong, Z.; Viswanathan, V. Design rules for liquid crystalline electrolytes for enabling dendrite-free lithium metal batteries. *Proc. Natl. Acad. Sci. U. S. A.* **2020**, *117*, 26672−26680.

(9) Kato, T. From nanostructured liquid crystals to polymer-based electrolytes. *Angew. Chem., Int. Ed.* **2010**, *49*, 7847−7848.

(10) Imrie, C. T.; Ingram, M. D.; McHattie, G. S. Ion transport in glassy side-group liquid crystalline polymer electrolytes. *Adv. Mater.* **1999**, *11*, 832−834.

(11) Sakuda, J.; Hosono, E.; Yoshio, M.; Ichikawa, T.; Matsumoto, T.; Ohno, H.; Zhou, H.; Kato, T. Liquid-crystalline electrolytes for lithium-ion batteries: Ordered assemblies of a mesogen-containing carbonate and a lithium salt. *Adv. Funct. Mater.* **2015**, *25*, 1206−1212.

(12) Ichikawa, T.; Yoshio, M.; Hamasaki, A.; Kagimoto, J.; Ohno, H.; Kato, T. 3D interconnected ionic nano-channels formed in polymer films: self-organization and polymerization of thermotropic bicontinuous cubic liquid crystals. *J. Am. Chem. Soc.* **2011**, *133*, 2163−2169.

(13) Kerr, R. L.; Edwards, J. P.; Jones, S. C.; Elliott, B. J.; Gin, D. L. Effect of varying the composition and nanostructure of organic carbonate-containing lyotropic liquid crystal polymer electrolytes on their ionic conductivity. *Polym. J.* **2016**, *48*, 635−643.

(14) Kerr, R. L.; Miller, S. A.; Shoemaker, R. K.; Elliott, B. J.; Gin, D. L. New type of Li ion conductor with 3D interconnected nanopores via polymerization of a liquid organic electrolyte-filled lyotropic liquid-crystal assembly. *J. Am. Chem. Soc.* **2009**, *131*, 15972−15973.

(15) Eisele, A.; Kyriakos, K.; Bhandary, R.; Schönhoff, M.; Papadakis, C. M.; Rieger, B. Structure and ionic conductivity of liquid crystals having propylene carbonate units. *J. Mater. Chem. A* **2015**, *3*, 2942−2953.

(16) Onuma, T.; Hosono, F.; Takenouchi, M.; Sakuda, J.; Kajiyama, S.; Yoshio, M.; Kato, T. Noncovalent approach to liquid-crystalline ion conductors: High-rate performances and room-temperature operation for Li-ion batteries. *ACS Omega* **2018**, *3*, 159−166.

(17) Zhang, G.; Chen, X.; Zhao, Y.; Ma, F.; Jing, B.; Qiu, H. Lyotropic liquid-crystalline phases formed by pluronic P123 in ethylammonium nitrate. *J. Phys. Chem. B* **2008**, *112*, 6578−6584.

(18) Wang, L.; Chen, X.; Chai, Y.; Hao, J.; Sui, Z.; Zhuang, W.; Sun, Z. Lyotropic liquid crystalline phases formed in an ionic liquid. *Chem. Commun.* **2004**, 2840−2841.

(19) Tunkara, E.; Albayrak, C.; Polat, E. O.; Kocabas, C.; Dag, Ö. Highly proton conductive phosphoric acid−nonionic surfactant lyotropic liquid crystalline mesophases and application in graphene optical modulators. *ACS Nano* **2014**, *8*, 11007−11012.

(20) Albayrak, C.; Cihaner, A.; Dag, Ö. A new, highly conductive, lithium salt/nonionic surfactant, lyotropic liquid-crystalline mesophase and its application. *Chem. - Eur. J.* **2012**, *18*, 4190−4194.

(21) Balcı, F.; Balcı, S.; Kocabas, C.; Dag, Ö. Lyotropic liquid-crystalline mesophase of lithium triflate−nonionic surfactant as gel electrolyte for graphene optical modulator. *J. Phys. Chem. C* **2017**, *121*, 11194−11200.

(22) Yılmaz, E.; Olutaş, E. B.; Barım, G.; Bandara, J.; Dag, Ö. Lithium salt−nonionic surfactant lyotropic liquid crystalline gel-electrolytes with redox couple for dye sensitized solar cells. *RSC Adv.* **2016**, *6*, 97430−97437.

(23) Soni, S. S.; Fadadu, K. B.; Gibaud, A. Ionic conductivity through thermoresponsive polymer gel: ordering matters. *Langmuir* **2012**, *28*, 751−756.

(24) Salikolimi, K.; Sudhakar, A. A.; Ishida, Y. Functional ionic liquid crystals. *Langmuir* **2020**, *36*, 11702−11731.

(25) Saat, G.; Balcı, F. M.; Alsaç, E. P.; Karadas, F.; Dag, Ö. Molten salt self-assembly: synthesis of mesoporous $LiCoO_2$ and $LiMn_2O_4$ thin films and investigation of electrocatalytic water oxidation performance of lithium cobaltate. *Small* **2018**, *14*, 1701913.

(26) Balci, F. M.; Karakaya, I.; Alsaç, E. P.; Yaman, M. Y.; Saat, G.; Karadas, F.; Ülgüt, B.; Dag, Ö. Synthesis of mesoporous $LiMn_2O_4$ and

$LiMn_{2-x}Co_xO_4$ thin films using the MASA approach as efficient water oxidation electrocatalysts. *J. Mater. Chem. A* **2018**, *6*, 13925−13933.
(27) Amirzhanova, A.; Karakaya, I.; Uzundal, C. B.; Karaoğlu, G.; Karadas, F.; Ülgüt, B.; Dag, Ö. Synthesis and water oxidation electrocatalytic and electrochromic behaviours of mesoporous nickel oxide thin film electrodes. *J. Mater. Chem. A* **2019**, *7*, 22012−22020.
(28) Amirzhanova, A.; Akmansen, N.; Karakaya, I.; Dag, Ö. Mesoporous $MnCo_2O_4$, $NiCo_2O_4$, and $ZnCo_2O_4$ thin-film electrodes as electrocatalysts for the oxygen evolution reaction in alkaline solutions. *ACS Appl. Energy Mater.* **2021**, *4*, 2769−2785.
(29) Çelik, Ö.; Dag, Ö. A new lyotropic liquid-crystalline phase is formed from oligo- (ethylene oxide) surfactants and $[M(H_2O)_n]X_m$, transition metal complexes. *Angew. Chem., Int. Ed.* **2001**, *40*, 3800−3803.
(30) Albayrak, C.; Soylu, A. M.; Dag, Ö. Lyotropic liquid-crystalline mesophases of [Zn(H2O)6](NO3)2−C12EO10−CTAB−H2O and [Zn(H2O)6](NO3)2−C12EO10−SDS−H2O systems. *Langmuir* **2008**, *24*, 10592−10595.
(31) Albayrak, C.; Özkan, N.; Dag, Ö. Origin of lyotropic liquid crystalline mesophase formation and liquid crystalline to mesostructured solid transformation in the metal nitrate salt− surfactant systems. *Langmuir* **2011**, *27*, 870−873.
(32) Rodriguez, C.; Kunieda, H. Effect of electrolytes on discontinuous cubic phases. *Langmuir* **2000**, *16*, 8263−8269.
(33) Klaus, A.; Tiddy, G. J. T.; Solans, C.; Harrar, A.; Touraud, D.; Kunz, W. Effect of salts on the phase behavior and the stability of nano-emulsions with rapeseed oil and an extended surfactant. *Langmuir* **2012**, *28*, 8318−8328.
(34) Mitchell, J. D.; Tiddy, G. J. T.; Waring, L.; Bostock, T.; McDonald, M. P. Phase behavior of polyethylene surfactants with water. Mesophase structures and partial miscibility (cloud points). *J. Chem. Soc., Faraday Trans. 1* **1983**, *79*, 975−1000.
(35) Sakya, P.; Seddon, J. M.; Templer, R. H.; Mirkin, R. J.; Tiddy, G. J. T. Micellar cubic phases and their structural relationships: The nonionic surfactant system $C_{12}EO_{12}$/water. *Langmuir* **1997**, *13*, 3706−3714.
(36) Hofmeister, F. Zur lehre von der wirkung der salze. *Naunyn-Schmiedeberg's Arch. Pharmacol.* **1888**, *25*, 1−30.
(37) Gibb, B. C. Hofmeister's curse. *Nat. Chem.* **2019**, *11*, 963−965.
(38) Zhang, Y.; Cremer, P. S. Interactions between macromolecules and ions: the Hofmeister series. *Curr. Opin. Chem. Biol.* **2006**, *10*, 658−663.
(39) Zhang, Y.; Furyk, S.; Bergbreiter, D. E.; Cremer, P. S. Specific ion effects on the water solubility of macromolecules: PNIPAM and the Hofmeister series. *J. Am. Chem. Soc.* **2005**, *127*, 14505−14510.
(40) Ashraf, H.; Guo, Y.; Wang, N.; Pang, S.; Zhang, Y. Hygroscopicity of Hofmeister salts and glycine aerosols−salt specific interactions. *J. Phys. Chem. A* **2021**, *125*, 1589−1597.
(41) Bruce, E. E.; Okur, H. I.; Stegmaier, S.; Drexler, C. I.; Rogers, B. A.; van der Vegt, N. F. A.; Roke, S.; Cremer, P. S. Molecular mechanism for the interactions of Hofmeister cations with macromolecules in aqueous Solution. *J. Am. Chem. Soc.* **2020**, *142*, 19094−19100.
(42) Okur, H. I.; Hladílková, J.; Rembert, K. B.; Cho, Y.; Heyda, J.; Dzubiella, J.; Cremer, P. S.; Jungwirth, P. Beyond the Hofmeister Series: Ion-Specific Effects on Proteins and Their Biological Functions. *J. Phys. Chem. B* **2017**, *121*, 1997−2014.
(43) Marcus, Y. Effect of ions on the structure of water: structure making and breaking. *Chem. Rev.* **2009**, *109*, 1346−1370.
(44) Gaiduk, A. P.; Galli, G. Local and global effects of dissolved sodium chloride on the structure of water. *J. Phys. Chem. Lett.* **2017**, *8*, 1496−1502.
(45) Kang, B.; Tang, H.; Zhao, Z.; Song, S. Hofmeister series: insights of ion specificity from amphiphilic assembly and interface property. *ACS Omega* **2020**, *5* (12), 6229−6239.
(46) Acharyya, A.; Mukherjee, D.; Gai, F. Assessing the effect of Hofmeister anions on the hydrogen-bonding strength of water via nitrile stretching frequency shift. *J. Phys. Chem. B* **2020**, *124*, 11783−11792.
(47) Moghaddam, S. Z.; Thormann, E. The Hofmeister series: Specific ion effects in aqueous polymer solutions. *J. Colloid Interface Sci.* **2019**, *555*, 615−635.
(48) Hribar, B.; Southall, N. T.; Vlachy, V.; Dill, K. A. Ions affect the structure of water. *J. Am. Chem. Soc.* **2002**, *124*, 12302−12311.
(49) Salis, A.; Ninham, B. W. Models, and mechanisms of Hofmeister effects in electrolyte solutions, and colloid and protein systems revisited. *Chem. Soc. Rev.* **2014**, *43*, 7358−7377.
(50) Jungwirth, P.; Tobias, D. J. Specific ion effects at the air/water interface. *Chem. Rev.* **2006**, *106*, 1259−1281.
(51) Richmond, G. L. Molecular bonding and interactions at aqueous surfaces as probed by vibrational sum frequency spectroscopy. *Chem. Rev.* **2002**, *102*, 2693−2724.
(52) Noah-Vanhoucke, J.; Smith, J. D.; Geissler, P. L. Statistical mechanics of sum frequency generation spectroscopy for the liquid−vapor interface of dilute aqueous salt solutions. *Chem. Phys. Lett.* **2009**, *470*, 21−27.
(53) Seki, T.; Sun, S.; Zhong, K.; Yu, C.-C.; Machel, K.; Dreier, L. B.; Backus, E. H. G.; Bonn, M.; Nagata, Y. Unveiling heterogeneity of interfacial water through the water bending mode. *J. Phys. Chem. Lett.* **2019**, *10*, 6936−6941.
(54) Seki, T.; Chiang, K.-Y.; Yu, C.-C.; Yu, X.; Okuno, M.; Hunger, J.; Nagata, Y.; Bonn, M. The Bending Mode of Water: A Powerful Probe for Hydrogen Bond Structure of Aqueous Systems. *J. Phys. Chem. Lett.* **2020**, *11*, 8459−8469.
(55) Greenspan, L. Humidity fixed points of binary saturated aqueous solutions. *J. Res. Natl. Bur. Stand., Sect. A* **1977**, *81A*, 89−96.
(56) Dag, Ö.; Alayoğlu, S.; Uysal, I. Effects of ions on the liquid crystalline mesophase of transition-metal salt:surfactant (C_nEO_m). *J. Phys. Chem. B* **2004**, *108*, 8439−8446.
(57) Sorenson, G. P.; Schmitt, A. K.; Mahanthappa, M. K. Discovery of a tetracontinuous, aqueous lyotropic network phase with unusual 3D-hexagonal symmetry. *Soft Matter* **2014**, *10*, 8229−8235.
(58) Albayrak, C.; Barim, G.; Dag, Ö. Lyotropic liquid crystal to soft mesocrystal transformation in hydrated salt-surfactant mixtures. *Chem. - Eur. J.* **2013**, *19*, 15026−15035.
(59) Topuzlu, E. Y.; Ulgut, B.; Dag, Ö. Role of water in the lyotropic liquid crystalline lithium iodide-iodine-water-$C_{12}E_{10}$ mesophase as a gel electrolyte in a dye-sensitized solar cell. *Langmuir* **2021**, *37*, 8305−8313.
(60) Ni, Y.; Skinner, J. L. IR and SFG vibrational spectroscopy of the water bend in the bulk liquid and at the liquid-vapor interface, respectively. *J. Chem. Phys.* **2015**, *143*, 014502.
(61) Falk, M. The frequency of the H-O-H bending fundamental in solids and liquids. *Speclrochimica Acta* **1984**, *40A*, 43−48.
(62) Ichikawa, T.; Yoshio, M.; Hamasaki, A.; Mukai, T.; Ohno, H.; Kato, T. Self-organization of room-temperature ionic liquids exhibiting liquid-crystalline bicontinuous cubic phases: Formation of nano-ion channel networks. *J. Am. Chem. Soc.* **2007**, *129*, 10662−10663.
(63) Lee, K.-K.; Park, K.-H.; Kwon, D.; Choi, J.-H.; Son, H.; Park, S.; Cho, M. Ion-pairing dynamics of Li^+ and SCN^- in dimethylformamide solution: Chemical exchange two-dimensional infrared spectroscopy. *J. Chem. Phys.* **2011**, *134*, 064506.
(64) Ji, M.; Hartsock, R. W.; Sung, Z.; Gaffney, K. J. Influence of solute-solvent coordination on the orientational relaxation of ion assemblies in polar solvents. *J. Chem. Phys.* **2012**, *136*, 014501.
(65) Fournier, J. A.; Carpenter, W.; De Marco, L.; Tokmakoff, A. Interplay of ion−water and water−water interactions within the hydration shells of nitrate and carbonate directly probed with 2D IR spectroscopy. *J. Am. Chem. Soc.* **2016**, *138*, 9634−9645.

https://doi.org/10.1021/acs.langmuir.1c02411
Langmuir 2021, 37, 14443−14453